Received: 23 October 2023 | Revised: 16 February 2024 | Accepted: 2 March 2024

DOI: 10.1111/ffe.14289

ORIGINAL ARTICLE

FFEMS Fatigue & Fracture of Engineering Materials & Structures WILEY

A meshfree approach for analyzing strain fields near crack tips from Digital Image Correlation displacement data

Giancarlo L. Gómez Gonzales[1] | **Alonso Camacho-Reyes**[1] | **Julián A. Ortiz González**[2] | **Francisco A. Díaz**[1]

[1]Departamento de Ingeniería Mecánica y Minera, University of Jaén, Jaén, Spain

[2]Central Hidroeléctrica de Caldas, CHEC, Caldas, Colombia

Correspondence
Giancarlo L. Gómez Gonzales, Departamento de Ingeniería Mecánica y Minera, University of Jaén, Jaén, Spain.
Email: glgomez@ujaen.es

Funding information
Ministerio de Universidades del Gobierno de España

Abstract

The element-free Galerkin (EFG) meshfree method is employed in this research to compute strain fields based on discrete displacement data obtained from digital image correlation (DIC). To validate the method's accuracy, both simulated images with highly heterogeneous deformations and real tests conducted on notched specimens with known solutions are initially employed. The study then investigates the strain field near the crack tip in an AISI 1020 steel specimen through a multiscale experiment. From the macroscale experiment, the strain data are used to determine the crack-tip plastic zone size, and the solution is compared with predictions from linear-elastic fracture mechanics. The stress intensity factor is also determined. Furthermore, the high strain gradient ahead of the crack tip is determined from the microscale experiment and compared against commercial DIC software. Experimental results confirm the effectiveness of the proposed formulation in crack tip analysis.

KEYWORDS

crack-tip field, digital image correlation, meshfree methods, strain measurements

Highlights

- Enhancing the calculation of strain fields is achieved through a meshfree formulation.
- The method is validated using simulated and experimental images with heterogeneous deformations.
- The large strain gradient near a fatigue crack tip is evaluated.

1 | INTRODUCTION

Digital image correlation (DIC) is a non-contact optical technique that enables full-field measurements of displacement and strain on the surface of a material undergoing mechanical deformation. It has become a widely employed experimental technique in solid mechanics, covering various length scales from microns

to meters.[1–3] Particularly, in the study of fatigue crack propagation,[4–8] DIC has found successful applications for investigating material fracture mechanisms, significantly expanding its use over the past decades. However, despite the robust performance shown by this method, characterizing the crack tip field, where significant strain variations occur over a short distance, may present challenges for the DIC algorithm. This is because of the requirement for high-magnification optics, a suitable speckle pattern, and illumination. Additionally, a robust algorithm is essential to effectively address the inherent noise of the DIC system itself.

In the DIC procedure, the deformation measurements are directly obtained by comparing digital images taken from the specimen surface during load application. In the last decades, formulations have been proposed to improve the strain calculation which depends strongly on the DIC software settings defined by the analyst.[9]

The output data from the correlation process consist of discrete displacements obtained by tracking small rectangular regions (called subsets) from the reference to the deformed image. More information about the DIC process can be found in the 2009 book authored by Sutton et al.[10] Once the displacement of each subset is obtained, the strains can be determined by numerical differentiation of the discrete displacement data. Unfortunately, numerical differentiation has the potential to amplify the noise present in the computed solution. Therefore, smoothing techniques based on polynomial fitting[11,12] and finite element approaches[13,14] are commonly used in post-processing routines. Many image-matching algorithms have been proposed to perform this task from the original work by Peters and Ranson.[15] The two main algorithms that researchers have thoroughly studied are the subset-based local DIC[16–18] and the finite element-based global DIC.[19–21]

Both methods have advantages and drawbacks depending on the application, being successfully incorporated into several commercial and academic software packages. This paper addresses the strain calculation procedure by using the element-free Galerkin (EFG) meshfree method.[22–26] The main goal of meshfree methods (also called meshless methods) is to eliminate the requirement for a predefined mesh by using nodes or points without connection between them to approximate the solution. The combination of DIC with meshfree methods for global deformation measurement was proposed by Andrianopoulos[27] in 2006. This first approach was based on the EFG method, which employs the moving least squares (MLS) approximation to construct the meshfree shape functions. In recent years, different formulations combining DIC and meshfree methods have been proposed. Gonzáles and Meggiolaro[28] proposed a new experimental-numerical technique that combines a feature-based matching technique with the EFG method to model the displacement field and its derivatives. The scattered nodes, obtained by matching corresponding key points in pairs of undeformed and deformed images, serve as the input data for the meshfree formulation. The technique shows effective performance in retrieving the strain distribution around a semicircular notch in a steel specimen under a bending load. Drahman et al.[29] developed a Meshfree-DIC technique that uses circular adhesive markers of constant size that are regularly distributed on the region of interest to track the specimen surface deformation. The algorithm uses the coordinates of each circular marker as nodes in the meshfree formulation. The applicability of the technique was tested through tensile tests on pure epoxy samples. Chen and Coppieters[30] developed a Meshfree-DIC algorithm also based on the EFG method. The analysis used synthetic images in which a grid of regularly distributed nodes was artificially added over the reference image. Groth et al.[31] proposed a meshfree-DIC algorithm for post-processing strain evaluation from large displacement. In this case, the meshfree formulation is based on radial basis functions. The method was numerically and experimentally tested for the case of drilled specimens. In general, the combination of DIC with meshfree methods exhibits robust capabilities in accurately capturing deformations and providing reliable results for various applications. However, experimental applications in fracture mechanics analyses are few; Zhu et al.[32] used a hybrid DIC–EFG method to calculate the stress intensity factor (K) based on the J-integral. For the J-integral calculation, the evaluation of the stresses and strains around a closed contour that encloses the crack tip is only required. This evaluation is accomplished through the application of strain–displacement equations and the generalized Hooke's law.

This paper aims to analyze the full-field crack tip solution, which requires high strain-gradient measurements. In the initial phase of this study, a meshfree formulation for strain calculation was implemented in Matlab based on the EFG method. The different steps involved in implementing the methodology are illustrated in Figure 1. Initially, displacement measurements are acquired through DIC processing, whether using subset-based DIC or another DIC approach. The discrete displacement data are subsequently utilized as input in the meshfree formulation, employing the measurement points as nodes in its formulation. No specific information is required a priori concerning DIC processing, such as subset size, step size (ST), or any other parameters used in the correlation procedure. Finally, the EFG

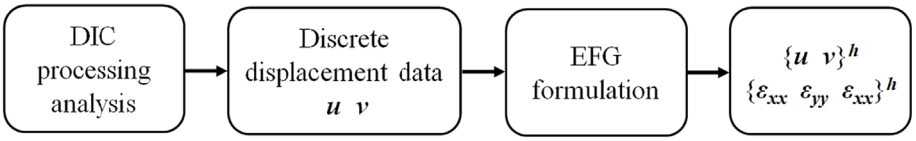

FIGURE 1 Workflow of the process used for strain calculation using the proposed meshfree formulation.

provides the approximated solution for the displacement fields, u^h and v^h, along with their derivatives. A version of this formulation is available for download at http://strainanalysisuja.es.

Initially, the performance of the algorithm is evaluated using simulated images from DIC Challenge image sets,[33] which consist of synthetic images under different deformation conditions. This dataset is offered by the International Digital Image Correlation Society (iDICs) and serves as a standardized benchmark for evaluating the performance of DIC algorithms. The solution provided is contrasted with results obtained from a commercial DIC software package, which is developed by Correlation Solution. Furthermore, real images obtained from a keyhole-notched specimen subjected to tensile loading were analyzed and compared with the numerical solution as part of the validation process.

Finally, a real test involving the analysis of the crack tip field was performed using a multiscale test. In the macroscale experiment, the assessment of the linear-elastic crack tip field involves determining the stress intensity factor and the monotonic plastic zone around the crack tip. For that, linear-elastic equations from the fracture mechanics were utilized. In the microscale experiment, the elastoplastic field near the crack tip was evaluated. Additionally, a commercial DIC software package (VIC-2D and VIC-3D from Correlated Solutions) was used to perform subset-based DIC with the purpose of comparison against those obtained with the proposed meshfree formulation. Furthermore, the stability and accuracy of the solution offered by the proposed method were assessed by examining its sensitivity to variations in the influence domain size.

2 | MESHFREE FORMULATION

The EFG method is one of the most widely used meshfree methods in solid mechanics. Other meshfree methods that have been developed are the diffuse element method,[34] the h-p clouds,[35] and meshfree local Petrov–Galerkin.[36] Within the EFG method, shape functions are constructed through the MLS approximation. The solution for the displacement component, u, at each node with local coordinates (x, y) is expressed as a weighted sum of the values of the request function at neighboring nodes within a support domain

$$u^h(\mathbf{x}) = \sum_i^n \phi_i(\mathbf{x}) u_i \tag{1}$$

where n is the number of nodes, ϕ the shape function related to the ith node, and u is the nodal displacements. Equation (1) can be written in a matrix form as given by

$$\Phi = \{\phi_1(\mathbf{x})\ \phi_2(\mathbf{x})\ \phi_3(\mathbf{x})\ \ldots\ \phi_n(\mathbf{x})\}^T \tag{2}$$

and

$$\mathbf{u} = \{u_1\ \ u_2\ \ u_3\ \ \ldots\ \ u_n\}^T \tag{3}$$

where Φ is the shape function matrix and u is the displacement vector for all ith nodes.

The shape functions are constructed within a local domain or group of selected nodes around the point of interest $\mathbf{x}$ using the MLS method. As shown in Figure 2, the influence domain controls the number of nodes used to support or approximate the field function value at $\mathbf{x}$ using Equation (2). Consequently, nodes outside the domain have no influence on the solution calculation. The shape of the local domain can have a variety of geometries, although a circular domain is more usual and practical. For this application, the displacement discontinuity due to a crack was modeled by changing the shape of the support domain, cutting the region located on the opposite side of the discontinuity. For that, some node searching algorithms[37] such as the visibility, transparency, and diffraction methods are available in the literature for solving problems that contain crack discontinuities. In the meshfree approach proposed here, a node-searching algorithm was implemented for improving the construction of approximations around the crack tip. As shown in Figure 2, the implemented routine reduces the influence of nodes within the support domain that contain a crack located on the opposite side of the crack. The implementation of this procedure begins with the essential step of locating the crack tip position in the DIC data. This is accomplished by following the methodology outlined in Vasco-Olmo et al.'s[38] analysis, where the crack tip is identified through the plotting of a series of profiles of vertical displacement perpendicular to the crack plane. The convergence of all profiles onto a single point indicates the precise location

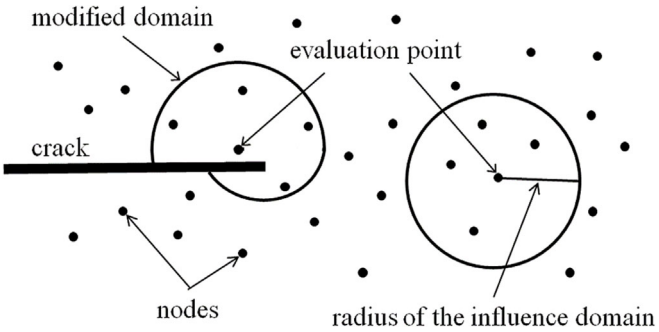

FIGURE 2 Examples of local support domain for the proposed EFG formulation.

where they intersect the crack plane, revealing the crack tip position. Subsequently, data points over the crack faces and the crack tip are excluded from the analysis. This exclusion is necessary to avoid unrealistic high strain values computes in these areas, arising from abrupt changes in displacement due to the opening or separation of the crack flanks during loading.

Furthermore, modifying the influence domain, as illustrated in Figure 2, proposes to minimize or mitigate strain calculations along the region of interest's border, where only half of the support domain is filled with data points. This would lead to less accurate strain calculations, commonly referred to as the border effect. Typically, these areas are not critical for analysis. However, in the presence of a crack generating a discontinuity in the region of interest, the edge effects can significantly impact the results.

2.1 | Shape function by MLS approximation

The MLS strategy to build the meshfree shape functions begins with a basic polynomial description:

$$u^h(\mathbf{x}) = \sum_{j=1}^{m} p_j(\mathbf{x}) a_j(\mathbf{x}) = \mathbf{p}^T(\mathbf{x})\mathbf{a}(\mathbf{x}) \tag{4}$$

where $\mathbf{p}(\mathbf{x})$ is the polynomial basis function (e.g., linear and quadratic), $\mathbf{a}(\mathbf{x})$ is a vector of unknown coefficients, and m is the number of terms. This expression can also be written in matrix forms

$$\mathbf{p}^T(\mathbf{x}) = \{p_1(\mathbf{x}) \;\; p_2(\mathbf{x}) \;\; p_3(\mathbf{x}) \;\; \ldots \;\; p_m(\mathbf{x})\}^T \tag{5}$$

and

$$\mathbf{a}(\mathbf{x}) = \{a_1(\mathbf{x}) \;\; a_2(\mathbf{x}) \;\; a_3(\mathbf{x}) \;\; \ldots \;\; a_m(\mathbf{x})\} \tag{6}$$

Minimizing the difference between the local approximation and the function allows for the determination of the unknown coefficients $\mathbf{a}(\mathbf{x})$. A weighted residual function of the expression can be constructed as follows:

$$H = \sum_i^n w(\mathbf{x}-\mathbf{x}_i)\left[u^h(\mathbf{x}) - u_i\right]^2 \tag{7}$$

where $w(\mathbf{x} - \mathbf{x}_i)$ is the weight function and n is the number of points in the local domain of a point of interest.

The weight function and its derivatives are required to be positive and continuous inside the local domain. This formulation adopted the exponential weight function,[39] which is frequently employed:

$$w(s)\begin{cases} e^{-(s/0.4)} & s \le 1 \\ 0 & s > 1 \end{cases} \tag{8}$$

The weight function depends on s, which is determined by

$$s = \frac{\|\mathbf{x}-\mathbf{x}_i\|}{\alpha \cdot dm} \tag{9}$$

where $\|\mathbf{x} - \mathbf{x}_i\|$ is the distance between the node $\mathbf{x}_i$ to the point of evaluation at $\mathbf{x}$ (center of the weight function), dm is the radius of the circular domain (as illustrated in Figure 1) that is defined by the user, and the α parameter is selected to ensure that the moment matrix A remains non-singular (usually $\alpha = 2$).

Furthermore, minimizing the weighted residuals H over an $(\mathbf{x})$ gives

$$\frac{\delta H}{\delta \mathbf{a}(\mathbf{x})} = 0 \tag{10}$$

which leads to

$$\mathbf{A}(\mathbf{x})\mathbf{a}(\mathbf{x}) = \mathbf{B}(\mathbf{x})\mathbf{U} \tag{11}$$

where $\mathbf{U}$ is the matrix of displacement, and

$$\mathbf{A}(\mathbf{x}) = \sum_{i=1}^{n} w(\mathbf{x}-\mathbf{x}_i)\mathbf{p}(\mathbf{x}_i)\mathbf{p}^{\mathbf{T}}(\mathbf{x}_i) \tag{12}$$

$$\mathbf{B}(\mathbf{x}) = \left[w(\mathbf{x}-\mathbf{x}_i)\mathbf{p}^{\mathbf{T}}(\mathbf{x}_i) \;\; w(\mathbf{x}-\mathbf{x}_i)\mathbf{p}^{\mathbf{T}}(\mathbf{x}_i) \;\; \ldots \;\; w(\mathbf{x}-\mathbf{x}_n)\mathbf{p}^{\mathbf{T}}(\mathbf{x}_n)\right] \tag{13}$$

Then, the coefficient vector, $\mathbf{a}(\mathbf{x})$, can be determined as

$$\mathbf{a}(\mathbf{x}) = \mathbf{A}^{-1}(\mathbf{x})\mathbf{B}(\mathbf{x})\mathbf{U} \tag{14}$$

By substituting Equation (14) into Equation (4), and comparing it with Equation (1), the following expressions can be obtained:

$$u^h(\mathbf{x}) = \underbrace{\mathbf{p}^{\mathbf{T}}(\mathbf{x})\mathbf{A}^{-1}(\mathbf{x})\mathbf{B}(\mathbf{x})}_{\Phi(x)}\mathbf{U} \tag{15}$$

$$\Phi(\mathbf{x}) = \mathbf{p}^{\mathbf{T}}(\mathbf{x})\mathbf{A}^{-1}(\mathbf{x})\mathbf{B}(\mathbf{x}) \tag{16}$$

2.2 | Strain calculation

Using Equation (4), the approximated displacements u^h and v^h (depicting the x and y-displacement field, respectively) can be defined as follows.

$$\begin{pmatrix} u \\ v \end{pmatrix}^h = \sum_i^n \begin{bmatrix} \phi_i & 0 \\ 0 & \phi_i \end{bmatrix} \begin{Bmatrix} u_i \\ v_i \end{Bmatrix} \tag{17}$$

By using the strain–displacement relation, the strain field at any position of $\mathbf{x}$ can be computed:

$$\begin{pmatrix} \varepsilon_x \\ \varepsilon_y \\ \varepsilon_{xy} \end{pmatrix}^h = \sum_i^n \begin{bmatrix} \frac{\delta}{\delta x} & 0 \\ 0 & \frac{\delta}{\delta y} \\ \frac{\delta}{\delta x} & \frac{\delta}{\delta y} \end{bmatrix} \begin{Bmatrix} u \\ v \end{Bmatrix}^h = \sum_i^n \begin{bmatrix} \frac{\delta\phi_i}{\delta x} & 0 \\ 0 & \frac{\delta\phi_i}{\delta y} \\ \frac{\delta\phi_i}{\delta x} & \frac{\delta\phi_i}{\delta y} \end{bmatrix} \begin{Bmatrix} u_i \\ v_i \end{Bmatrix} \tag{18}$$

In accordance with Equation (18), the strain field components require the first derivatives of the MLS shape function. Additional information regarding implementation aspects of meshfree methods can be found in Liu and Gu[24] and Nguyen et al.[25]

3 | VALIDATION OF THE MESHFREE FORMULATION

3.1 | Simulated experiments results

To evaluate the performance of the proposed meshfree formulation, artificially generated images with heterogeneous deformation were used. Specifically, images from the DIC Challenge[40] were employed, focusing on two sets known as Sample 14 and Sample 15, which exhibit varying types of strain gradients. The analysis of these images represents a notable challenge because achieving high strain resolution to capture peak values is difficult when dealing with rapidly changing strain values over a short distance. The deformed images were generated by the imposition of unidirectional displacement functions applied along a single axis (x or y), with no displacement imposed on the other axis.

Sample 14 consists of three cases of numerically deformed images denoted as L1, L3, and L5. These images have dimensions of 2048 × 588 pixels and were created by applying a unidirectional sinusoidal displacement field along the x-axis, with increasing frequency. In the case of the Sample 15 dataset, a unidirectional displacement field along the y-axis was numerically imposed. For this analysis, the image denoted as P200_K400 that has dimensions of 2000 × 1000 pixels was used. This image features three distinct and well-separated strain peaks with sharp discontinuities, similar to the high-strain gradients typically observed near notches or cracks. In both analyses, the DIC displacement data were computed using the subset-based DIC approach with a subset size of 31 × 31 pixels and a ST of 10 pixels. Consequently, for Sample 14, the region of interest consists of a grid with 52 × 199 evaluation points, while for Sample 15, it consists of a grid with 97 × 185 evaluation points.

For comparison purposes, the strain solution computed using the VIC-2D software is also considered. In subset-based algorithms, the strain window (SW) parameter indicates the number of subsets used to compute a single strain measurement. Additionally, the extent of the region over which strains are computed is defined by the virtual strain gage (VSG).[9] This VSG calculation relies on user-defined DIC parameters, particularly the SW and ST. Mathematically, the VSG is calculated as VSG = [(SW − 1) × ST] + 1.

The values of the dm parameter used for strain calculation in the meshfree formulation are presented in Table 1. Additionally, the table includes the SW parameters employed by the subset-based DIC algorithm and their corresponding VSG size. The optimal parameters for each analysis shown in Table 1 were determined through a trial and error approach. During this procedure, it was verified that large domains provide a smoothed solution with low peak strain resolution, while small domain sizes result in a solution sensitive to noise. However, it is worth noting that high-strain gradients require small support domains to perform accurate approximations. The analysis of this set of images aims to

emphasize the trade-off between noise reduction and spatial resolution.

In Figures 3 and 4, the results of the calculated solutions are plotted in comparison to the expected strain values. Figure 3 displays the outcomes for the Sample 14, while Figure 4 depicts the results for the Sample 15. As the imposed displacement field is unidirectional, the corresponding strain value remains the same for every line (column or row) in the image. Therefore, the line cut result represents the mean value of the 201 rows along the horizontal axis for the Sample 14 analysis. In the case of the Sample 15 analysis, the line cut result represents the mean value of the 188 columns corresponding to the vertically imposed displacement. To provide a clearer view of the error associated with strain calculations, the bias error and the standard deviation of the strain solutions along the line cut were also plotted. The bias error indicates the offset from the known value of the measured variable, primarily resulting from the spatial filtering of the DIC algorithms. The standard deviation represents the dispersion of data points around the mean value calculated for each row along the horizontal axis.

TABLE 1 Parameters used for strain calculation.

Image	Meshfree	Subset-based DIC
Sample 14/Image L1	$dm = 200$ px	SW = 15 VSG = 141 px
Sample 14/Image L3	$dm = 100$ px	SW = 7 VSG = 61 px
Sample 14/Image L5	$dm = 50$ px	SW = 5 VSG = 41 px
Sample 15/K400	$dm = 50$ px	SW = 5 VSG = 41 px

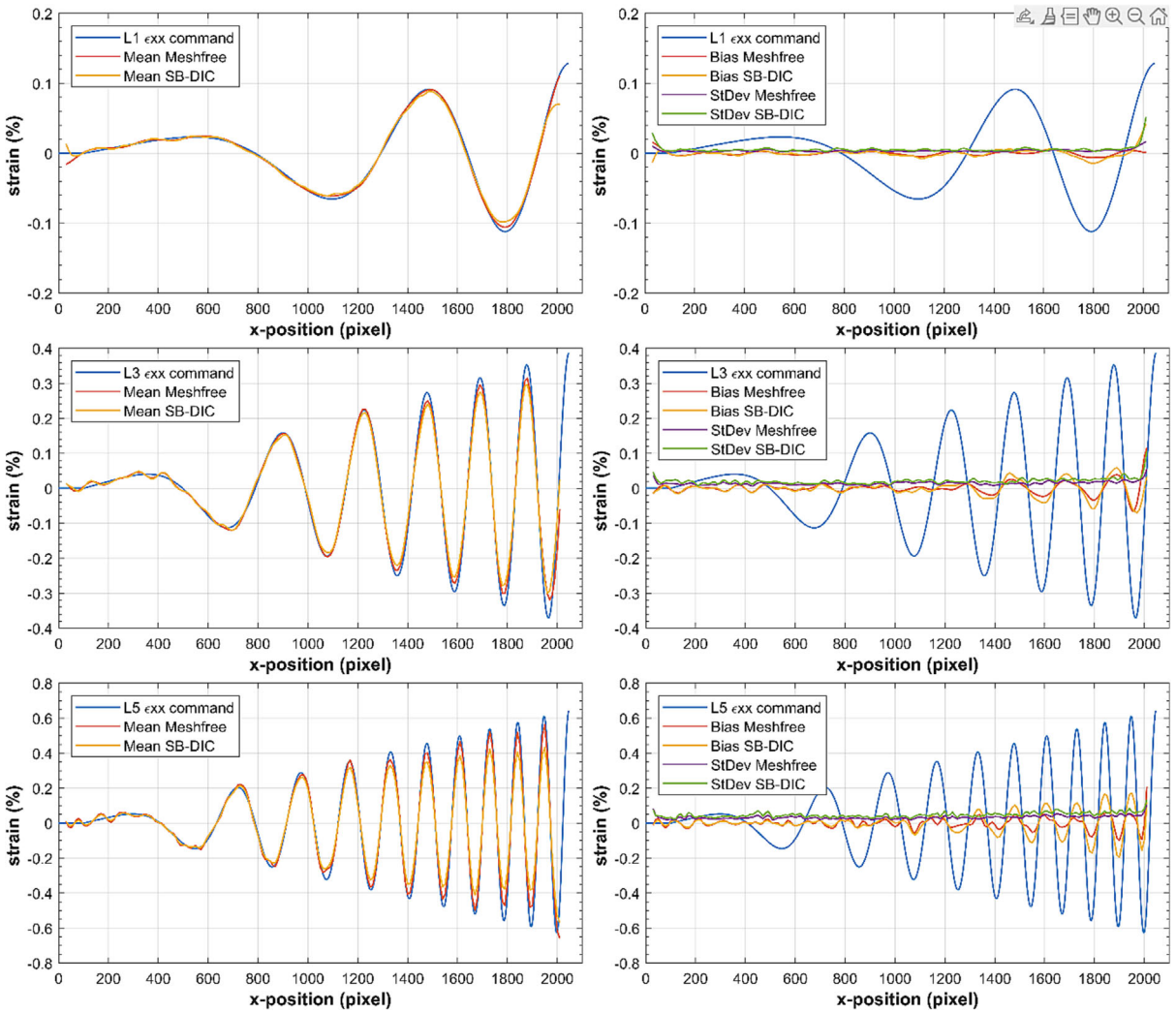

FIGURE 3 Experimental results for the analysis of sample 14 with meshfree formulation and subset-based DIC (SB-DIC). [Colour figure can be viewed at wileyonlinelibrary.com]

It can be observed that all the experimental results closely match the commanded values. In the Sample 14 analysis, it is expected that the strain solution becomes noisier as the frequency and amplitude of the imposed strain field increase along the *x*-direction. However, reducing the domain size allows the meshfree formulation to more accurately reproduce the high-frequency strain information.

In the case of the Sample 15 analysis, the meshfree formulation performs well in reproducing strains in the lower region of the strain gradient. As the strain approaches its maximum value, there is a rapid change in strain values over a short distance. In this region, the meshfree solution reproduced approximately 93% of the strain gradient. Capturing the peak strain is challenging, primarily because the values of zero strain on the opposite side of the strain gradient significantly impact both the approximation and its derivative.

A comprehensive analysis of these results indicates that the meshfree strain solutions exhibit the lower bias error, surpassing the subset-based DIC method in capturing the strain peak. Additionally, supporting these findings, Table 2 presents a summary of the averaged standard deviations and RMSE values, illustrating the overall quality of the meshfree strain solution across the four cases.

3.1.1 | Sensitivity analysis of the dm parameter

A feature of DIC algorithms is the dependence of the strain solution on the size of the region over which the calculation is performed. As stated by Reu,[9] DIC algorithms operate as a non-linear filtering operation with low-pass attributes, influenced by DIC parameters. If the region is too small, it yields noisy measurements, while excessively large regions tend to smooth the strain fields. Similar effects are anticipated when adjusting the support domain, *dm*, in the meshfree formulation, which determines the number of evaluation points utilized for strain solution. To evaluate the influence of the *dm* parameter, the strain solution for Sample 14 L1, computed with a *dm* of 200 pixels, was compared with solutions obtained at both 25% and 50% higher and lower *dm* values. The results of this analysis are presented in Figure 5, while Table 3 provides an overview of the standard deviation and RMSE analysis. As anticipated, it is evident that the strain results exhibit more noise for smaller *dm* sizes. In contrast, increasing the *dm* size tends to flatten the solution in gradient areas, although resulting in lower standard deviation values. It can be seen that the solution with a *dm* of 200 pixels appears to achieve a better balance between noise and smoothing.

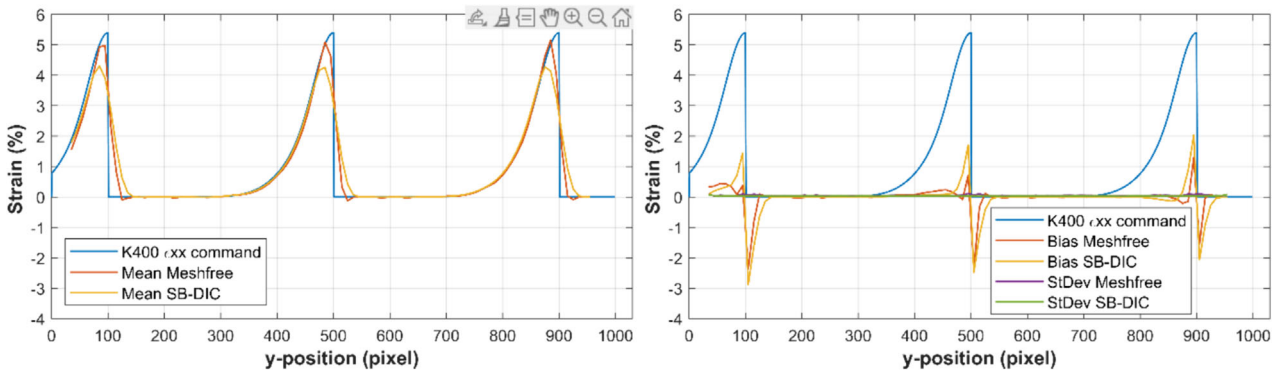

FIGURE 4 Experimental results for the analysis of sample 15 with meshfree formulation and subset-based DIC (SB-DIC). [Colour figure can be viewed at wileyonlinelibrary.com]

Image	StDev meshfree	StDev SB-DIC	RMSE Meshfree	RMSE SB-DIC
Sample 14/Image L1	0.0042	0.0074	0.0032	0.0061
Sample 14/Image L3	0.0155	0.0225	0.0179	0.0213
Sample 14/Image L5	0.0349	0.0401	0.0303	0.0588
Sample K400	0.0360	0.0318	0.4359	0.6217

TABLE 2 Standard deviation and RMSE for the strain data shown in Figures 3 and 4.

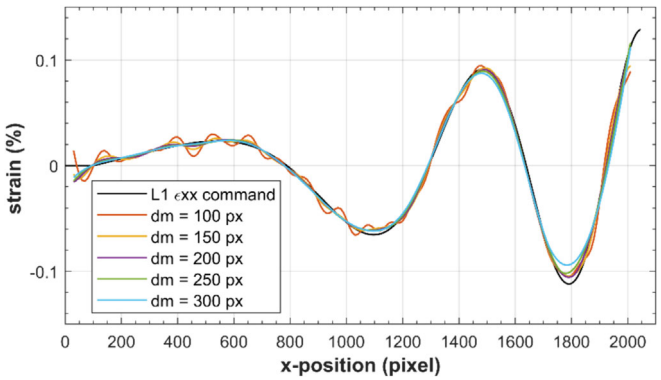

FIGURE 5 Experimental results for the analysis of sample 14 L1 with different values of *dm*. [Colour figure can be viewed at wileyonlinelibrary.com]

TABLE 3 Standard deviation and RMSE for the strain data shown in Figure 5.

dm parameter	StDev	RMSE
$dm = 100$ px	0.0043	0.0132
$dm = 150$ px	0.0064	0.0039
$dm = 200$ px	0.0042	0.0032
$dm = 250$ px	0.0028	0.0039
$dm = 300$ px	0.0021	0.0057

For a more comprehensive understanding of the findings presented in Table 3, Figure 6 assesses the error by examining the proximity of the data to the 45° reference line that indicates perfect alignment between the numerical and experimental data. Additionally, the 95% prediction confidence interval, equivalent to twice the standard deviation, for the results obtained with a *dm* of 200 pixels, is depicted by dashed lines on either side of the 45° reference line. It can be seen that most of the data for the *dm* values of 150 and 250 pixels fall inside the 95% prediction confidence interval, showing a good balance between noise and spatial filtering.

3.2 | Real experiment results

The performance of the meshfree formulation was assessed through a tensile test performed on a keyhole-shaped specimen made of steel API 5L Gr. B. The specimen, as shown in Figure 7, has a thickness of 4.8 mm. The material properties are listed in Table 4, which were obtained experimentally from a tensile test. To enable the DIC technique, one side of the specimen was coated with a random speckle pattern. The images were acquired using a stereoscopic system that consisted of two 5-megapixel cameras (Point Grey GRAS-50S5M), achieving a pixel resolution of approximately 11.5 μm/pixel for this test.

The analysis was conducted on the deformed image obtained under a load of 9.9 kN. Displacement data were obtained through DIC analysis using the subset-based DIC approach with a subset size of 19 pixels and an ST of 6 pixels. The resulting displacement data consist of a grid with 121×211 evaluation points. In the analysis, two different values of the *dm* parameter were tested: $dm = 0.75$ and $dm = 1$ mm.

Figure 8 displays the full-field strain solution for the ε_{yy} strain component obtained using the meshfree formulation. As illustrated in this figure, the application of a 9.9-kN tensile force induced a strain gradient around the notch, with a pronounced concentration of plastic deformation exceeding 0.7%. This indicates that the EFG formulation presented here can effectively capture the material's nonlinear behavior. Furthermore, it is shown that the meshfree solution demonstrated robust stability, with clearly defined contour lines representing the different levels of strain within the gradient.

Additionally, a numerical simulation of the problem was performed by using a 3D FEM model created in ANSYS. Figure 9 plots strain distributions, both the numerical and experimental, for the ε_{yy} strain component along a line on the *x*-axis. As observed, both solutions exhibit a similar trend. Moreover, the solutions provided from the meshfree formulation, with different values of *dm*, show a consistent concordance with minimal variation between them, suggesting a good balance between noise and spatial filtering. It's worth noting that the lack of strain data at the notch boundary is due to the limitations of the DIC correlation procedure. Subset-based DIC algorithms track subsets by considering the center of each subset as the measurement point. Therefore, for subsets located at the boundary, the displacement data are obtained at a distance from the notch boundary equivalent to half the size of the subset.

4 | CHARACTERIZATION OF THE STRAIN CRACK TIP FIELD BASED ON THE MESHFREE FORMULATION

A fatigue crack growth test was performed using a disk-shaped compact tension specimen made of AISI 1020 steel. Two stereoscopic systems, each with different optical magnifications, were placed on opposite sides of the cracked specimen (see Figure 10). The primary objective of this test is to determine the high strain gradient that develops around the crack tip. The geometry and specimen dimensions are shown in Figure 11. In addition, the material properties are provided in Table 5.

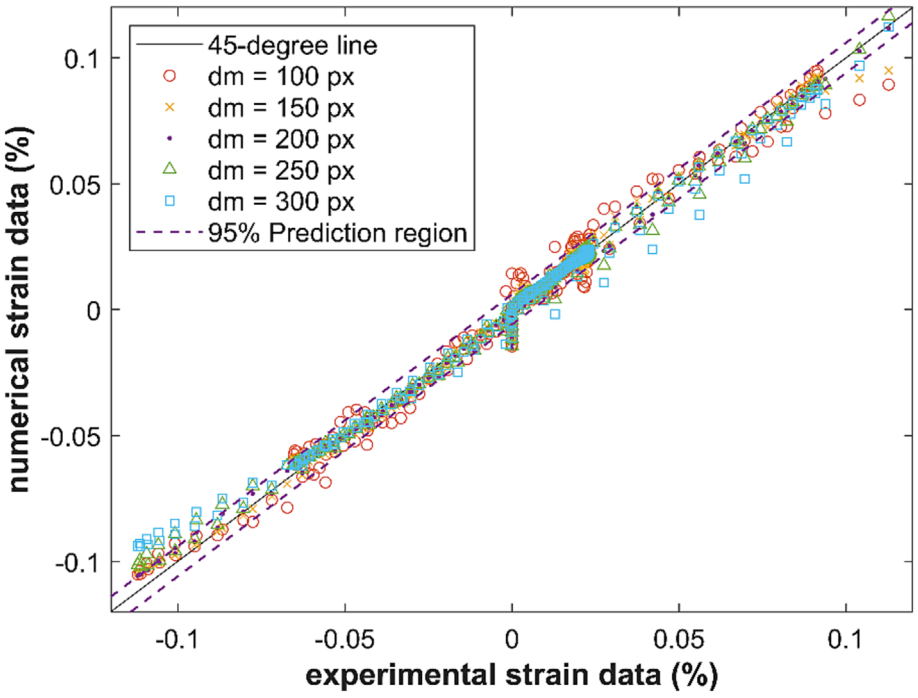

FIGURE 6 Comparison between numerical and experimental data for the analysis of sample 14 L1 with different values of *dm*. [Colour figure can be viewed at wileyonlinelibrary.com]

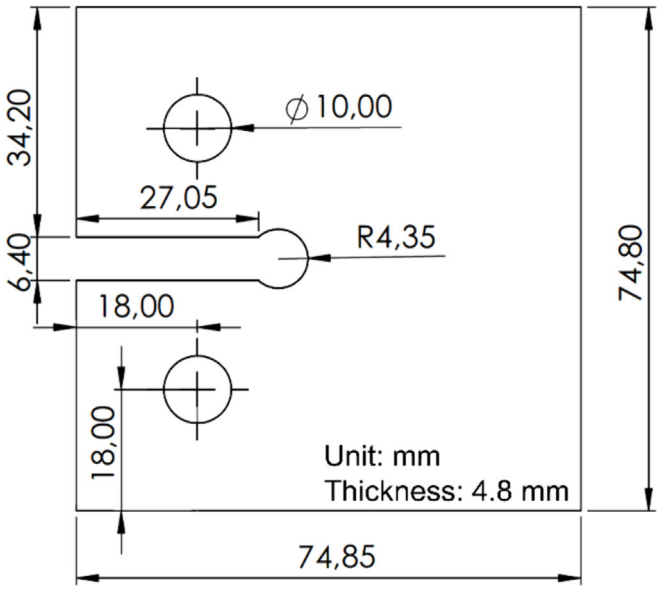

FIGURE 7 Dimensions of the keyhole-notched specimen.

For the macroscale magnification, a pair of 5-megapixel cameras (Point Grey GRAS-50S5M) were used in a stereo configuration. This setup achieved a pixel resolution of approximately 9.85 μm/pixel. For the microscale magnification, a stereo microscope (Olympus SZX16) was located on the other side of the specimen. The spatial resolution for the microscale experiment was about 1.6 μm/pixel. All images collected using two DIC systems were processed using the VIC-3D software.

Initially, a fatigue crack was allowed to propagate with a $\Delta K = 20$ MPa$\sqrt{m}$. Once the crack had reached a length of 10 mm, a new $\Delta K = 30$ MPa$\sqrt{m}$ was applied. Images of the specimen were captured during the loading cycle immediately following the application of the higher ΔK range.

TABLE 4 Material properties for the steel API 5L Gr. B.

Parameter	Value	Unit
Young modulus, E	171.1	GPa
0.2% yield stress, σ_y	301.8	MPa
Ultimate stress, σ_u	501	MPa

In the macroscale experiment, DIC displacement data were acquired through correlation analysis using a subset size of 31 pixels and an ST of 10 pixels. This DIC displacement data are subsequently employed to compute strain values utilizing the meshfree formulation. Two different *dm* parameter values were investigated: $dm = 1$ mm and $dm = 1.5$ mm. Therefore, displacement and strain components are calculated from Equation 18. In the initial stage, the stress intensity factor is determined. For that, it can be extracted from the local elastic strain or displacement field, measured at the surface around the crack tip, through a fitting process to theoretical solutions for strain, or displacement fields. In this case, the Westergaard equations were employed for the solutions.

Figure 12 illustrates the calculation of ΔK values for different loads across the loading cycle, ranging from the minimum to the maximum loading. It is worth noting that the DIC analysis utilizes the image captured at minimum loading as the reference. Consequently, the ΔK

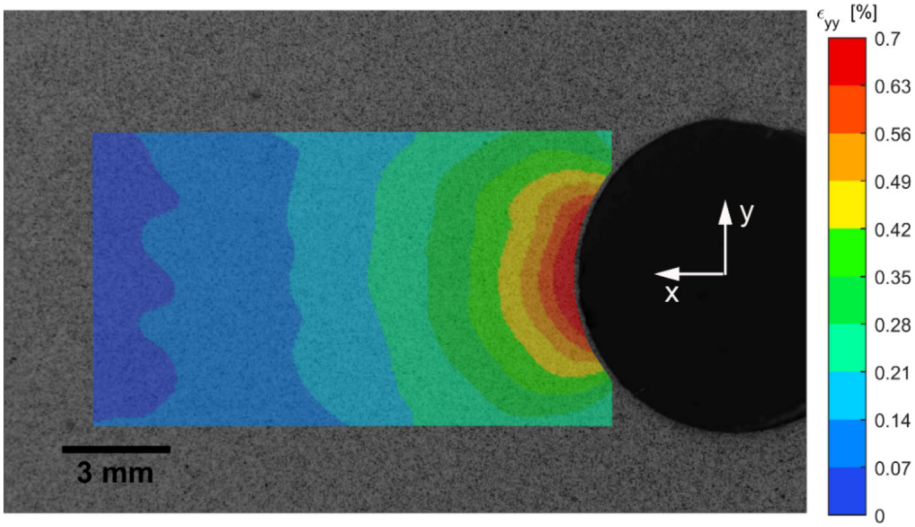

FIGURE 8 Strain map results in the *y*-direction under a 9.9-kN load obtained from the meshfree formulation with $dm = 1$ mm. [Colour figure can be viewed at wileyonlinelibrary.com]

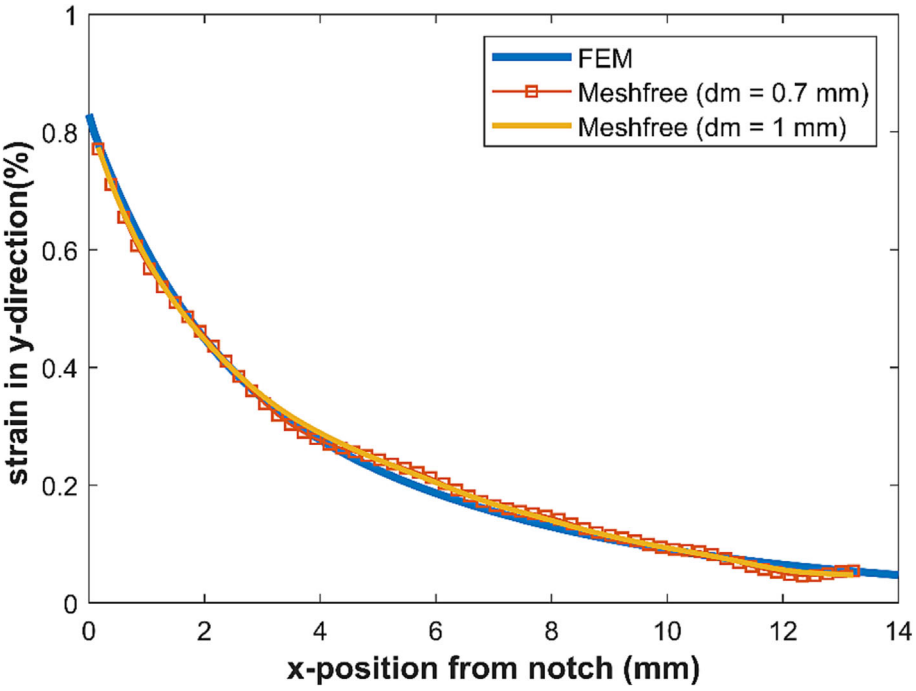

FIGURE 9 Comparison between experimental solutions for the distribution of vertical strains along the *x*-position ahead of the notch. [Colour figure can be viewed at wileyonlinelibrary.com]

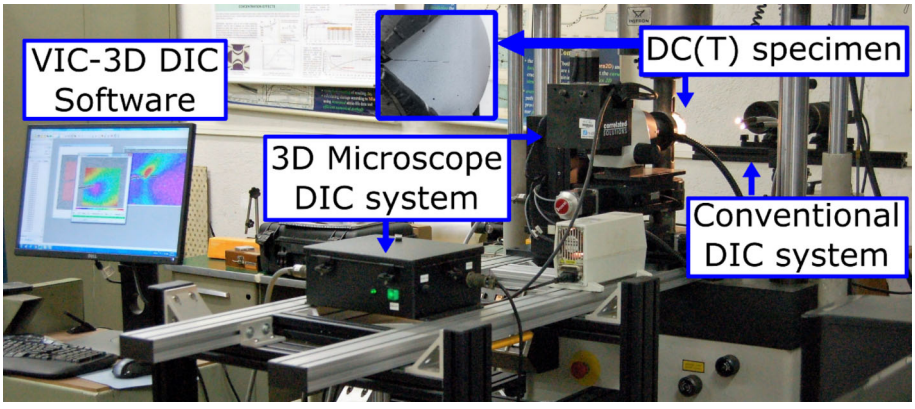

FIGURE 10 Experimental multiscale setup used for investigation. [Colour figure can be viewed at wileyonlinelibrary.com]

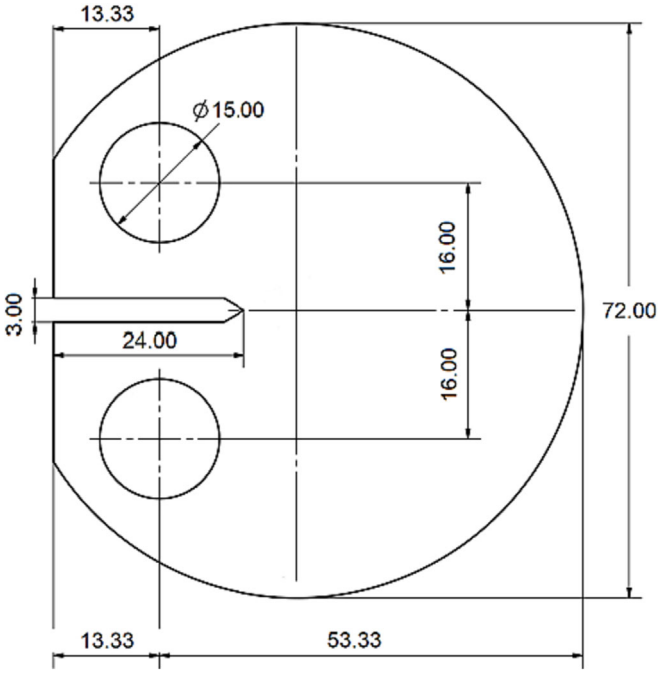

FIGURE 11 Dimensions of the disk-shaped compact tension specimen with a thickness of 5 mm (all dimensions are in mm).

TABLE 5 Material properties for the steel AISI 1020 steel.

Parameter	Value	Unit
Young's modulus, E	206	GPa
0.2% yield stress, σ_y	285	MPa

value at minimum loading is zero. From the experimental results, it can be observed that the ΔK values at maximum loading match with the imposed ΔK of 30 MPa√m. Moreover, it is observed that there is no evidence of plasticity-induced crack closure behavior. Therefore, the determined ΔK values exhibit a linear increase as the loading progresses and remain consistently aligned with the ASTM standard even with an increase in the *dm* value. The absence of the crack closure effects is attributed to the introduction of the new ΔK value, which exceeds significantly the previous value. This results in the blunting of the crack tip during the initial cycles after its application. The phenomenon of crack blunting enables the crack to stay open, even under low loads, temporarily mitigating the effects of crack closure. Hence, comparing with the ASTM standard value is feasible at this stage, given the absence of crack closure effects.

The second part of the analysis involves determining the plastic zone size using the obtained full-field strain maps. Hence, once the strain components have been determined, the corresponding stresses can be calculated

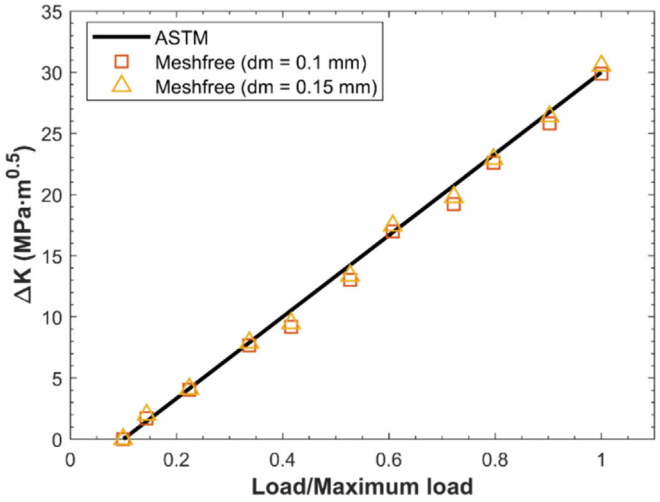

FIGURE 12 Stress intensity factor calculation results. [Colour figure can be viewed at wileyonlinelibrary.com]

using Hooke's law. The von Mises equivalent stress is then computed from the stress tensor. Subsequently, the plastic zone size is established by identifying the points where the von Mises stress exceeds the yield stress of the material. Thus, the elastoplastic border surrounding the crack tip is determined solely based on the linear-elastic stresses.[38,41]

Figure 13 displays the comparison between the experimental data obtained with two different *dm* values and the estimation of the plastic zone based on Weestergaard equations. Notably, there is concordance between theoretical and experimental results, along with minor alterations observed when increasing the *dm* value from 1 to 1.5 mm. Both analyses performed to determine the stress intensity factor and crack-tip plastic zone size using the provided meshfree solution demonstrate the effectiveness of the formulation in accurately characterizing the linear-elastic crack tip field.

Additionally, Figure 14 illustrates the resulting von Mises strain map using determined strain components with a *dm* value of 1 mm, employing a principal plane strain formulation that specifically accounts for surface strains within the analysis. Thus,

$$\varepsilon_{vMises} = \frac{2}{3}\sqrt{\varepsilon_1^2 - \varepsilon_1\varepsilon_2 + \varepsilon_2^2} \tag{19}$$

where ε_1 and ε_2 are the principal strains.

As observed in this figure, a crack promotes a severe strain concentrator adjacent to its tip. The macroscale experiment is useful to observe the behavior of the surrounding crack tip field. As the strain increases to its maximum value ahead of the crack tip, a large change in strain values is expected within a small distance. To

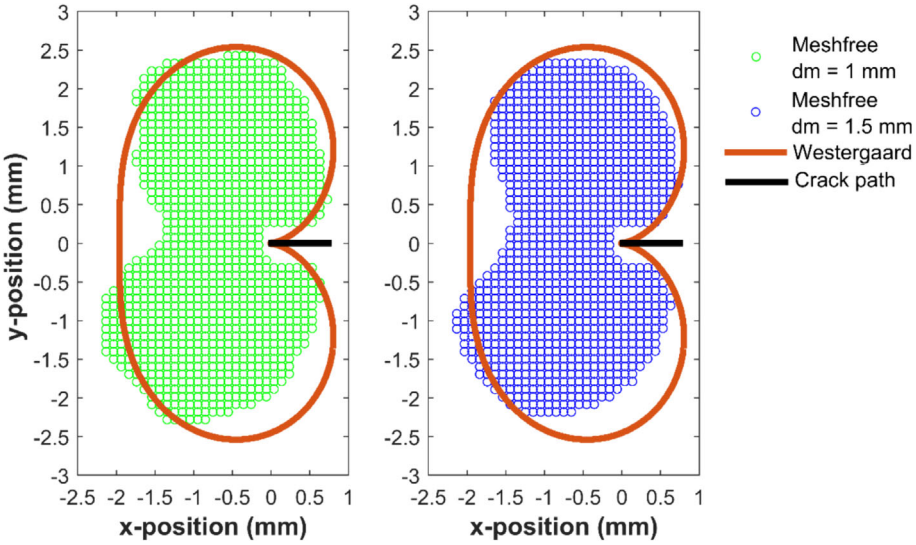

FIGURE 13 Comparison between experimental and theoretical results for determining the plastic zone size. [Colour figure can be viewed at wileyonlinelibrary.com]

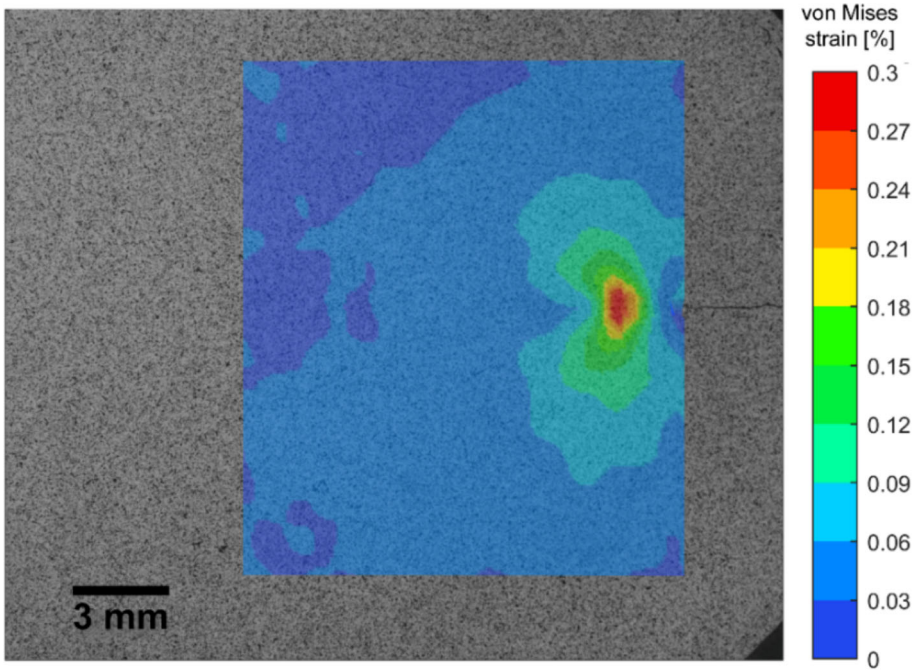

FIGURE 14 Macroscale experiment: results of the full-field strain map around the crack tip for a crack length of 10 mm under $\Delta K = 30$ MPa$\sqrt{m}$ obtained from the meshfree formulation with $dm = 1$ mm. [Colour figure can be viewed at wileyonlinelibrary.com]

characterize this material behavior, a higher resolution is required. For that, the images captured from the stereo microscope system were analyzed.

In the microscale experiment, DIC displacement data were collected by analyzing images with a subset size of 41 pixels and an ST of 10 pixels. Upon identifying the crack tip, the data points over the crack faces and the crack tip were manually excluded from the analysis to prevent their inherently higher noise level caused by abrupt displacement changes at the crack faces. This displacement data are then used to calculate the strain field around the crack tip using the meshfree formulation. Additionally, the strain solution provided by the VIC-3D software was computed for comparison purposes.

Figure 15 illustrates the comparison between the results for the von Mises strain calculated along the x-axis ahead of the crack tip using Equation 19. In this figure, the strain distributions with variations in dm and SWs parameter values for the meshfree formulation and the subset-based DIC approach, respectively, are presented. Decreasing the dm and SW parameter values results in more pronounced noise in the strain solutions, particularly observed in the low-strain gradient area, as detailed in Figure 15. The analysis shows that the subset-based DIC solution exhibits a slight increase in noise compared to the meshfree solution. Considering the influence of the support domain on the strain calculation, the selection of the parameter

that produces appropriate results can be likened to finding a balance between reducing measurement noise and avoiding data over-smoothing at the high-strain gradient region.

As depicted in Figure 15A, for the meshfree formulation, a convergence between curves in the high-strain gradient region is evident for dm values of 0.1 and 0.125 mm. The solution with $dm = 0.15$ mm appears smoother, whereas the solution with $dm = 0.075$ mm is noisier. Therefore, the solutions obtained with a dm value of 0.1 and 0.125 mm offer the most balanced compromise between noise and data smoothing. On the other hand, in Figure 15B, the curves obtained from the subset-based DIC software show no convergence in the high-strain gradient region. Furthermore, there is considerable variability between maximum strain values when compared with the results from the meshfree formulation. Close to the crack tip region, the meshfree formulation outperformed the flattened solution provided by the DIC software due to border effects, delivering a more consistent solution for this region. This highlights the capacity of the meshfree formulation to adjust the influence domain size effectively when dealing with discontinuities, such as cracks, within the analyzed region. These observations underscore the robustness of the meshfree formulation in handling challenging strain gradients, providing a valuable alternative for crack tip field analysis.

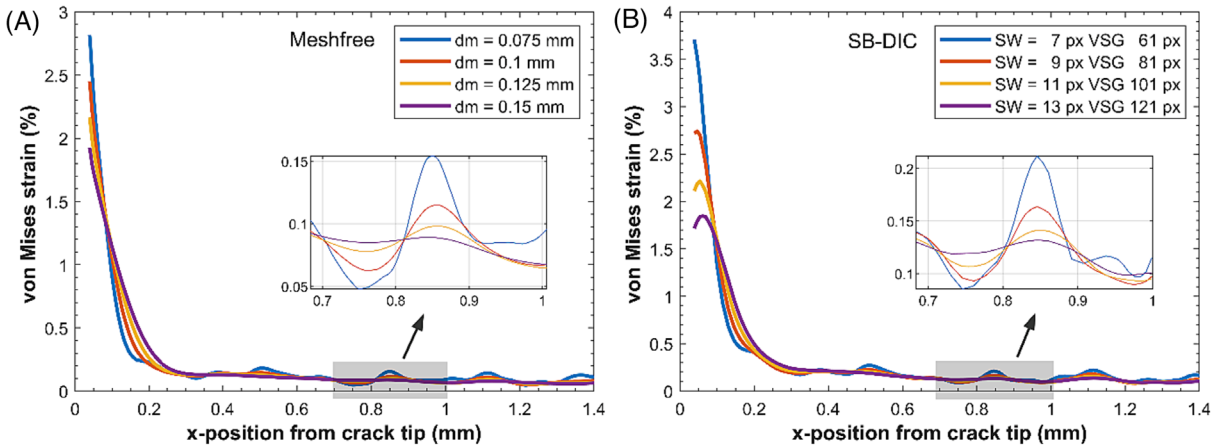

FIGURE 15 Comparison between von mises strain distributions along the x-axis obtained for (A) meshfree formulation and (B) subset-based DIC approach. [Colour figure can be viewed at wileyonlinelibrary.com]

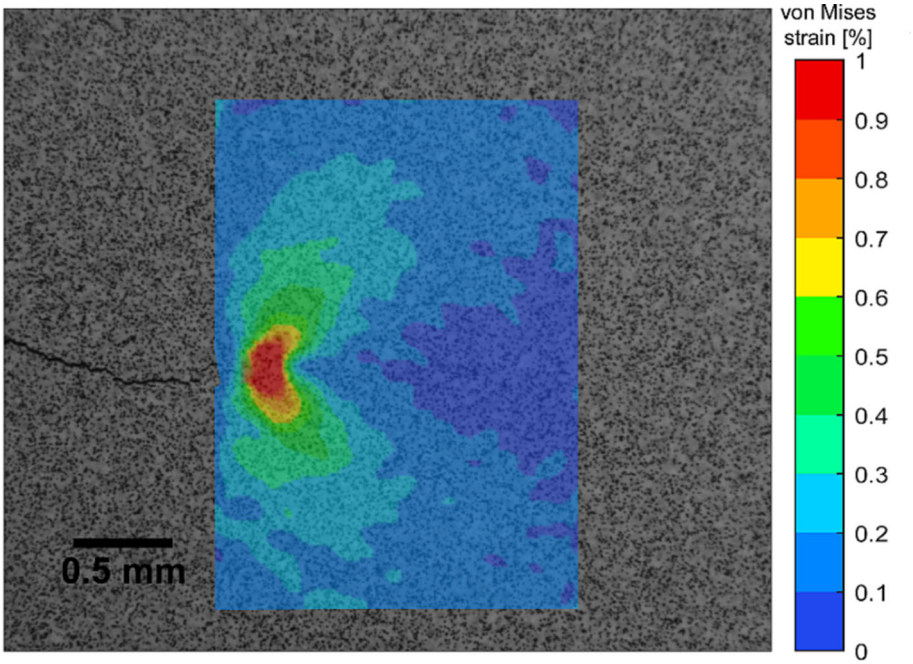

FIGURE 16 Microscale experiment: results of the full-field strain map around the crack tip for a crack length of 10 mm under $\Delta K = 30$ MPa$\sqrt{m}$ obtained from the meshfree formulation with $dm = 0.01$ mm. [Colour figure can be viewed at wileyonlinelibrary.com]

The von Mises strain map using the *dm* value of 0.1 mm is illustrated in Figure 16. It can be observed that the meshfree solution displayed remarkable stability, as evidenced by its clearly defined contour lines outlining the plastic lobes surrounding the crack tip. Therefore, the proposed meshfree formulation suggests a potential to enhance the accuracy of strain measurements, particularly in the region ahead of the crack tip where large errors in strain calculation are susceptible to occur, thus contributing to more reliable and robust analyses.

Finally, it is important to emphasize that the identification of the crack tip location constitutes a critical step in the methodology, which is performed prior to the analysis. Nonetheless, the sensitivity to the crack tip's position can be mitigated through the implementation of procedures for its accurate location, as previously mentioned.

5 | CONCLUSIONS

This paper assesses an evaluation of a meshfree approach implemented to extract the strain field surrounding a fatigue crack tip. Accurately characterizing the high strain gradient near crack tips holds significant importance in fracture mechanics, as it plays a crucial role in assessing material behavior and predicting crack propagation. Validation of the formulation involved both simulated and real image data. In simulated tests, highly non-uniform deformations in images with known solutions from the DIC challenge were used. Additionally, real test images were employed to examine the strain gradient of a keyhole-notched specimen subjected to tensile loading and compared with numerical simulation results. The findings demonstrate the stability of the solution provided by the proposed formulation when high-strain measurements were required, highlighting a favorable equilibrium between noise and data smoothing. Furthermore, the formulation was applied to analyze the crack tip field of a DCT specimen made of 1020 steel through a multiscale experiment. The proposed formulation successfully reproduced the strain crack tip field from the macroscale experiment. It accurately determined the stress intensity values and the size of the plastic zone from the linear-elastic strain solution. In the microscale experiment, the proposed formulation effectively handling both low and high strain gradient areas within the same analysis. Although, determining the optimal influence domain size for each analysis is still subject to the experience of the analyst. A significant level of agreement between solutions with different influence domain sizes was observed in the high-strain gradient region, ensuring their convergence. Analyzing the strain noise and avoiding excessive data smoothing lead to favorable outcomes. These findings emphasize the reliability and accuracy of the meshfree formulation in capturing rapidly changing strain values over short distances. Furthermore, additional improvements can be introduced to the formulation, demonstrating its potential to enhance the precision of crack tip field analysis.

ACKNOWLEDGMENTS

The authors would like to acknowledge the financial support from Ministerio de Universidades del Gobierno de España through the program "Recualificación del Sistema Universitario Español 2021-2023: ayudas Maria Zambrano."

DATA AVAILABILITY STATEMENT

The data that support the findings of this study are available from the corresponding author upon reasonable request.

NOMENCLATURE

$\mathbf{a}(x)$	coefficient vector
A, B	coefficient matrix
DIC	digital image correlation
dm	influence domain
E	Young modulus
EFG	element-free Galerkin
H	weighted residual function
FEM	finite element method
K	stress intensity factor
MLS	moving least squares
$\mathbf{p}(x)$	polynomial basis function
s	weight function parameter
ST	step size
SW	strain window size
u, v	displacement components
u^h, v^h	approximated displacement components
U	displacement matrix
VSG	virtual strain gage
$w(x)$	weight function
α	scaling parameter
ε	strain
$(\varepsilon_x, \varepsilon_y, \varepsilon_{xy})$	approximated strain components
$(\varepsilon_x, \varepsilon_y, \varepsilon_{xy})^h$	approximated strain components
ϕ	shape function
Φ	shape function matrix
ΔK	stress intensity factor range
σ	stress

ORCID

Alonso Camacho-Reyes https://orcid.org/0000-0002-7524-0039

Francisco A. Díaz https://orcid.org/0000-0003-0467-542X

REFERENCES

1. Sutton MA, Matta F, Rizos D, et al. Recent progress in digital image correlation: background and developments since the 2013 W M Murray lecture. *Exp Mech*. 2017;57(1):1-30.
2. Casperson MC, Carroll JD, Lambros J, Sehitoglu H, Dodds RH. Investigation of thermal effects on fatigue crack closure using multiscale digital image correlation experiments. *Int J Fatigue*. 2014;61:10-20.
3. Mehdikhani M, Steensels E, Standaert A, Vallons KAM, Gorbatikh L, Lomov SV. Multi-scale digital image correlation for detection and quantification of matrix cracks in carbon fiber composite laminates in the absence and presence of voids controlled by the cure cycle. *Compos Part B Eng*. 2018;154:138-147.
4. Vormwald M, Hos Y, Freire JLF, Gonzáles GLG, Díaz JG. Variable mode-mixity during fatigue cycles–crack tip parameters determined from displacement fields measured by digital image correlation. *Frattura ed Integrità Strutturale*. 2017;11(41):314-322.
5. Freire JLF, Paiva VEL, Gonzáles GLG, et al. Fatigue assessment and monitoring of a dented pipeline specimen. In: *American Society of Mechanical Engineers, pressure vessels and piping division (publication) PVP*. Vol.1; 2019.
6. Camacho-Reyes A, Vasco-Olmo JM, Gómez Gonzales GL, Diaz FA. Study of effective stress intensity factor through the CJP model using full-field experimental data. *Materials*. 2023;16:5705.
7. Gómez Gonzales GL, Vasco-Olmo JM, Antunes FV, Neto DM, Díaz FA. Experimental analysis of the plastic CTOD to characterize the variable amplitude fatigue crack growth in Grade 2 titanium samples. *Int J Fatigue*. 2023;174:107728.
8. Becker TH, Thorsten Becker CH. Extracting fracture properties from digital image and volume correlation displacement data: a review. *Strain*. 2023; 1.
9. Reu P. Virtual Strain Gage Size Study. Virtual strain gage size study. *Exp Tech*. 2015;39(5):1-3.
10. Sutton MA, Orteu JJ, Schreier HW. *Image correlation for shape, motion and deformation measurements*. Springer US; 2009.
11. Pan B, Asundi A, Xie H, Gao J. Digital image correlation using iterative least squares and pointwise least squares for displacement field and strain field measurements. *Opt Lasers Eng*. 2009;47(7-8):865-874.
12. Wang Z, Zhu P, Liu L, Zhou X. An accurate and robust strain field smoothing method based on polynomial fitting and anisotropic diffusion in digital image correlation. *Measurement*. 2023;113947.
13. Sutton MA, Turner JL, Bruck HA, Chae TA. Full-field representation of discretely sampled surface deformation for displacement and strain analysis. *Exp Mech*. 1991;31(2):168-177.
14. Yoneyama S. Smoothing measured displacements and computing strains utilising finite element method. *Strain*. 2011;47(s2):258-266.
15. Peters WH, Ranson WF. Digital imaging techniques in experimental stress. *Analysis*. 1982;21:427-431. doi:10.1117/127972925
16. Bruck HA, McNeill SR, Sutton MA, Peters WH. Digital image correlation using Newton-Raphson method of partial differential correction. *Exp Mech*. 1989;29(3):261-267.
17. Lu H, Cary PD. Deformation measurements by digital image correlation: implementation of a second-order displacement gradient. *Exp Mech*. 2000;40(4):393-400.
18. Pan B, Li K. A fast digital image correlation method for deformation measurement. *Opt Lasers Eng*. 2011;49(7):841-847.
19. Cheng P, Sutton MA, Schreier HW, McNeill SR. Full-field speckle pattern image correlation with B-spline deformation function. *Exp Mech*. 2002;42(3):344-352.
20. Sun Y, Pang JHL, Wong CK, Su F. Finite element formulation for a digital image correlation method. *Appl Optics*. 2005;44(34):7357-7363.
21. Besnard G, Hild F, Roux S. "Finite-element" displacement fields analysis from digital images: application to Portevin-Le Châtelier bands. *Exp Mech*. 2006;46(6):789-803.
22. Belytschko T, Lu YY, Gu L. Element-free Galerkin methods. *Int J Numer Methods Eng*. 1994;37(2):229-256.
23. Dolbow J, Belytschko T. An introduction to programming the meshfree element f reeGalerkin method. *Arch Comput Methods Eng*. 1998;5(3):207-241.
24. Liu GR, Gu YT. An introduction to meshfree methods and their programming. In: *An Introduction to Meshfree Methods and Their Programming*; 2005:1-479.
25. Nguyen VP, Rabczuk T, Bordas S, Duflot M. Meshfree methods: a review and computer implementation aspects. *Math Comput Simul*. 2008;79(3):763-813.
26. Liu GR. *Meshfree Methods: Moving Beyond thbe Finite Element Method*. Second ed; 2009:1-749.
27. Andrianopoulos NP. Full-field displacement measurement of a speckle grid by using a mesh-free deformation function. *Strain*. 2006;42(4):265-271.
28. Gonzáles G, Meggiolaro M. Strain field measurements around notches using SIFT features and meshfree methods. *Appl Optics*. 2015;54(14):4520-4528.
29. Drahman SH, Zainal Abidin AR, Kueh ABH. Two-dimensional meshfree-based digital image correlation for strain-displacement measurement. *Exp Tech*. 2022;46(2):273-286.
30. Chen B, Coppieters S. Meshfree digital image correlation using element free Galerkin method: theory, algorithm and validation. *Exp Mech*. 2023;63:517-528.
31. Groth C, Chiappa A, Porziani S, Biancolini ME, Marotta E, Salvini P. A post-processing method based on radial basis functions for the fast retrieval of the strain field in digital image correlation methods. *Materials*. 2022;15:7936.
32. Zhu Z, Luo S, Feng Q, Chen Y, Wang F, Jiang L. A hybrid DIC–EFG method for strain field characterization and stress intensity factor evaluation of a fatigue crack. *Measurement*. 2020;154:107498.
33. Reu PL, Toussaint E, Jones E, et al. DIC challenge: developing images and guidelines for evaluating accuracy and resolution of 2D analyses. *Exp Mech*. 2018;58(7):1067-1099.
34. Nayroles B, Touzot G, Villon P. Generalizing the finite element method: diffuse approximation and diffuse elements. *Comput Mech*. 1992;10(5):307-318.
35. Duarte A, Tinsley Odent J. H-p clouds-an h-p meshfree method. *Comput Methods Appl Mech Eng*. 1996;139(1):237-262.
36. Atluri SN, Zhu T. A new meshfree local Petrov-Galerkin (MLPG) approach in computational mechanics. *Comput Mech*. 1998;22(2):117-127.

37. Garg S, Pant M. Meshfree methods: a comprehensive review of applications. 2018;15. doi:10.1142/S0219876218300015
38. Vasco-Olmo JM, James MN, Christopher CJ, Patterson EA, Diaz FA. Assessment of crack tip plastic zone size and shape and its influence on crack tip shielding. *Fatigue Fract Eng Mater Struct*. 2016;39(8):969-981.
39. Belytschko T, Krongauz Y, Fleming M, Organ D, Liu WKS. Smoothing and accelerated computations in the element free Galerkin method. *J Comput Appl Math*. 1996;74(1-2):111-126.
40. https://idics.org/challenge/
41. Gonzáles GLG, González JAO, Paiva VEL, Freire JLF. Crack-tip plastic zone size and shape via DIC. In: *Fracture, Fatigue, Failure and Damage Evolution, Volume 6: Proceedings of the 2018 Annual Conference on Experimental and Applied Mechanics*. Springer International Publishing; 2019:5-10.

How to cite this article: Gómez Gonzales GL, Camacho-Reyes A, Ortiz González JA, Díaz FA. A meshfree approach for analyzing strain fields near crack tips from Digital Image Correlation displacement data. *Fatigue Fract Eng Mater Struct*. 2024;47(6):1994-2009. doi:10.1111/ffe.14289